PCCP

Accepted Manuscript

ROYAL SOCIETY OF CHEMISTRY

www.rsc.org/pccp

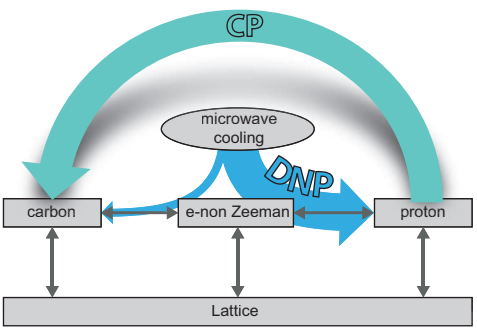

Investigation of DNP CP using a spin-thermodynamic model and optimization of CP in power-limited DNP probes using adiabatic RF pulses.

Cross Polarization for Dissolution Dynamic Nuclear Polarization

Michael Batel[a], Alexander Däpp[a], Andreas Hunkeler[a], Beat H. Meier[a], Sebastian Kozerke[b], and Matthias Ernst[a]*

[a] Physical Chemistry, ETH Zürich, Wolfgang-Pauli-Strasse 10, 8093 Zürich, Switzerland

[b] Institute for Biomedical Engineering, University and ETH Zürich, Gloriastrasse 35, 8092 Zürich, Switzerland

Corresponding Author:

Matthias Ernst
Physical Chemistry, ETH Zürich, Wolfgang-Pauli-Strasse 10, 8093 Zürich, Switzerland
e-mail: maer@ethz.ch
Telephone: +41 44 63 24366

Keywords: Dynamic Nuclear Polarization, Thermal Mixing, Cross Polarization, Adiabatic Excitation Pulses, Dissolution DNP, Adiabatic Demagnetization, Adiabatic Remagnetization

Abstract

Dynamic nuclear polarization (DNP) in combination with subsequent dissolution of the sample allows the detection of low-γ nuclei in solution state with a signal gain of tens of thousands compared to experiments starting from Boltzmann conditions. The long polarization build-up times of typically more than one hour are a drawback of this technique. The combination of dissolution DNP with cross-polarization (CP) in the solid state was shown to have the potential to overcome this disadvantage. In this article we discuss the cross-polarization step under dissolution DNP conditions in more detail. We show that adiabatic half-passage pulses allow us to enhance the CP efficiency in power-limited DNP probes. As a low-power alternative to Hartmann-Hahn CP we also demonstrate the applicability of frequency-swept de- and re-magnetization pulses for polarization transfer via dipolar order. We investigate implications and restrictions of the common solid-state DNP mechanisms to the DNP–CP technique and apply a spin-thermodynamic model based on the thermal-mixing mechanism. The model allows us to investigate the dynamics of the polarization levels in a system with two nuclear Zeeman reservoirs and explains the enhanced DNP efficiency upon solvent deuteration within a spin-thermodynamic picture.

1. Introduction

Dynamic nuclear polarization (DNP)[1] of solid samples at low temperatures in combination with subsequent dissolution using a hot solvent (dissolution DNP) as introduced by Ardenkjær-Larsen in 2003[2] has led to a renaissance of DNP in NMR and MRI.[3-5] Especially in the field of biomedical MRI the resulting signal enhancement of up to several ten thousand has enabled the detection of ^{13}C-labeled metabolites in relatively low concentration in-vivo with spatial, temporal, and spectral resolution.[3, 6-8]

The usual protocol of a dissolution DNP experiment includes the polarization process occurring around 1.3 K in a dedicated polarizer.[2, 9, 10] This process, excluding the time for sample preparation and cool down of the system takes approximately 1.5 to more than 2 hours for typical sample compositions that yield the highest polarization results, i.e., trityl-radical based samples. The polarization build up obtained with the TEMPO radical or its derivatives is usually faster by approximately one order of magnitude. Such samples yield, however, lower maximum polarization values on the target ^{13}C nuclei.[11, 12] With the aim of achieving maximum ^{13}C sensitivity, dissolution DNP experiments are usually conducted using the trityl radical, accepting the long polarization times and, thus, time- and planning-intensive experiments.

The use of cross polarization[13] under dissolution DNP conditions, first suggested by Linde[14] and Jannin et al.,[15] is a feasible approach to reduce the long polarization times. In this experiment, the TEMPO radical is used to polarize the ^{1}H nuclei and prior to dissolution a polarization transfer from ^{1}H to ^{13}C is applied in the solid state. The experimental implementation of cross polarization and dissolution to the liquid state requires modifications to the standard dissolution polarizer setup to allow sufficiently long strong pulses on two channels. Such a setup was first described by Linde[14] and by our group.[16] The advantage of this approach is an increase in the ^{13}C polarization by a factor of 2-3 and a speed up of the polarization build-up time compared to direct ^{13}C DNP (using trityl as a radical) in the same sample. However, the polarization levels achievable using TEMPO and CP are unlikely to reach the ones achieved in trityl-based samples in standard polarizers operating at 1.3 K and 3.4 T. Jannin et al. have recently shown that an increase in magnetic field to 6.7 T allows to close this gap.[17, 18]

As indicated previously[16] the dissolution DNP–CP experiment creates additional demands on the cryogenic probe design and on the timing of the dissolution protocol used in DNP–CP. The primary obstacle to overcome is the need for sufficiently high radio-frequency (rf) fields on the proton and carbon channel for an efficient CP transfer. This is difficult to implement experimentally due to increased arcing probability in the helium atmosphere found in flow-type cryogenic probes. In our work we use adiabatic half-passage pulses[19, 20] instead of conventional hard 90° excitation pulses to improve the efficiency of the CP transfer at low rf-power levels. Additionally, we explore the use of polarization transfer via dipolar order using frequency-swept low-power pulses. This approach is a variation of the amplitude-modulated adiabatic polarization transfer[21] and was suggested by Lee et al. for liquid-crystalline and solid samples.[22, 23]

The second important requirement in dissolution DNP–CP experiments is the minimization of the time between the polarization transfer and the start of the dissolution process. This is a consequence

of the thermal-mixing process, which is the DNP mechanism most suitable for these experiments as we show in a qualitative discussion in the *Theory* section. By applying an empirical spin-thermodynamic model, we show that one can explain many phenomena using this thermal-mixing model including the time dependence of the polarization of both ^{13}C and ^{1}H nuclei during the course of the experiment. In addition, the thermodynamic model correctly describes the enhanced DNP efficiency upon solvent deuteration. The experiments were carried out on a home-built DNP probe that is also briefly characterized in this article.

2. Theory

Since Overhauser suggested in 1953[24] to enhance the nuclear polarization of metals by saturating the EPR line, several similar mechanisms for nuclear polarization enhancement have been proposed, all utilizing microwave irradiation. Today, they are summarized together as DNP mechanisms. In the solid state, the DNP literature distinguishes three different mechanisms: The *solid effect* (SE), the *cross effect* (CE), and *thermal mixing* (TM).[25]

The solid effect was the first DNP mechanism in non-conducting solids proposed by Jeffries in 1957[26] and later experimentally demonstrated by Abragam and Proctor.[27] It is a two-spin effect between an electron and nuclear spin that relies on a strong anisotropic hyperfine interaction and well-separated single-, zero-, and double-quantum transitions. Therefore, a prerequisite for the SE is an electron-spin resonance (ESR) line that is narrow compared to the nuclear Zeeman frequency, i.e., $\Delta\omega_\mathrm{e} < \omega_\mathrm{n}$ (well-resolved SE) or the absence of strong spectral diffusion and a mainly inhomogeneous ESR line if $\Delta\omega_\mathrm{e} > \omega_\mathrm{n}$ (differential SE).[1] A rigorous mathematical treatment of the effect[1, 28] shows that the polarization enhancement, $\mathrm{defined\ as}\ \epsilon = P/P_{equ}\ \mathrm{is\ proportional\ to}\ \gamma_\mathrm{e}/\gamma_\mathrm{n}$, where γ_e and γ_n are the gyromagnetic ratios of the electrons and nuclei, respectively.

The cross effect is a three-spin process of a coupled system of two electron and one nuclear spin with the restriction of a mainly inhomogeneous ESR line with $\Delta\omega_\mathrm{e} > \omega_\mathrm{n}$ so that it is possible for the frequencies of the two electrons to fulfill the condition $|\omega_\mathrm{e,a} - \omega_\mathrm{e,b}| \approx \omega_\mathrm{n}$. A quantum-mechanical treatment and a comparison to the SE has been presented by Hovav et al..[29]

It is important to note that the combination of DNP with subsequent CP will not lead to an increase in the maximum polarization for DNP mechanisms where the polarization enhancement $\epsilon \propto \gamma_\mathrm{e}/\gamma_\mathrm{n}$. In these cases, the best a CP transfer could achieve would be to reach the same level of polarization as direct DNP can achieve. Due to the usually faster DNP build up for high-γ nuclei, however, the DNP–CP technique can be used to reduce the overall build-up time for the low-γ nuclei, as it is routinely done in MAS-DNP experiments where both CE and SE play an important role.[30, 31]

The thermal-mixing mechanism uses a spin-thermodynamic framework to explain the polarization transfer from electrons to nuclei.[32] The spin-temperature hypothesis states that a spin system isolated from the lattice and experiencing spin-spin interactions approaches a state of internal equilibrium characterized by a Boltzmann distribution of the population of its states, $p_i \propto \exp\left(\frac{-E_i}{k_\mathrm{B}T_s}\right)$. This distribution defines the spin temperature T_s and the inverse spin temperature $\beta_\mathrm{S} = (k_\mathrm{B}T_\mathrm{S})^{-1}$ of the system. For a system with multiple nuclear species, TM DNP uses a model that assigns unique spin

temperatures to the different nuclear Zeeman reservoirs, the electron Zeeman and to an additional electron non-Zeeman reservoir. The latter arises from all contributions to the electron Hamiltonian leading to ESR line broadening that commute to first order with the electron Zeeman Hamiltonian. The TM DNP mechanism can be described as a two-step process:

i. *Dynamic cooling/heating* is the process where the spin temperature of the electron non-Zeeman reservoir is being altered from thermal equilibrium by microwave irradiation.

ii. *Thermal mixing* is the process where the spin temperatures of the nuclear Zeeman reservoirs equilibrate with the one of the electron non-Zeeman reservoir. The necessary coupling between the reservoirs is only possible if $\omega_{\mathrm{n}} < \Delta\omega_{\mathrm{e}}$ to allow energy-conserving thermal contact. The thermal mixing step implies that the final spin temperatures (and with this the polarization enhancement) is independent of the nuclear gyromagnetic ratio and thus equal for all participating nuclear species. Only nuclei that fulfill the condition $\omega_{\mathrm{n}} < \Delta\omega_{\mathrm{e}}$ participate in the thermal-mixing process.

Note that the equilibration of the spin temperature of two spin systems having unlike gyromagnetic ratios, $\beta_n = \beta_m$, yields a situation in which their spin polarizations $P_i \propto \gamma_i \cdot \beta_i$ (in high-temperature approximation) differ by a factor of $\gamma_{\mathrm{m}}/\gamma_{\mathrm{n}}$. Such a situation is both met in the thermal equilibrium, where $\beta_m = \beta_n = \beta_L$ and in an enhanced state where both spin systems are enhanced by the same factor $\epsilon = \frac{P_i}{P_{equ}} = \beta_i/\beta_L$, with the lattice temperature $\beta_L = (k_{\mathrm{B}}T_{\mathrm{S}})^{-1}$.

While a detailed treatment of the cooling process is given by Abragam and Goldman[1] and has recently been reformulated by Goertz et al.,[33] to the best of our knowledge, the nature of the electron non-Zeeman reservoir has not been described in detail. In addition, the physical process enabling the coupling between the electron non-Zeeman reservoir and the nuclear Zeeman reservoirs has also not been treated in detail in the literature.

In our work, the TEMPO radical is used for DNP in concentrations around 50 mM where the resulting ESR line in the solid state is broader than the proton Larmor frequency. Even though the major contribution to this broadening is the *g*-anisotropy,[34] the dipolar electron-electron interactions are assumed to add homogeneous line broadening enabling spectral spin diffusion. Shimon et al.[35] have shown that the cross effect contributes only little to the overall DNP enhancement at temperatures below 10 K. Furthermore, the results presented here as well as experiments conducted on similar systems[11] show that the final spin temperature in such TEMPO-based systems is very similar for all nuclear species with $\omega_{\mathrm{n}} < \Delta\omega_{\mathrm{e}}$. Since the thermal-mixing mechanism does not only assume $\omega_{\mathrm{n}} < \Delta\omega_{\mathrm{e}}$ but also predicts equal spin temperature for all participating nuclear spin species, it is, thus, assumed to be the dominant DNP mechanism in the experiments presented here.

To get a semi-quantitative insight into the dynamics of such a system with multiple coupled spin reservoirs we use a thermodynamic model similar to the one suggested by Goldman.[36] Note that such a spin-temperature model describes only the interdependence of the various reservoirs (e.g., nuclear Zeeman baths, electron Zeeman bath, electron non-Zeeman bath) characterized by spin temperatures experiencing thermal mixing but neither the physical processes underlying such a model nor the mechanism leading to the dynamic cooling of the electron non-Zeeman reservoir.

Figure 1 shows the reservoirs included in our model: the lattice *L* (with inverse spin temperature β_L), the proton and carbon Zeeman reservoirs *HZ* and *CZ* (β_H and β_C, respectively), the electron non-Zeeman reservoir *NZ* (β_e), and an imaginary cooling reservoir *CL* (β_{CL}). The latter one is a virtual, physically non-existing reservoir to simulate the process of dynamic cooling by microwave irradiation. The two nuclear Zeeman reservoirs *HZ* and *CZ* are both coupled through the electron non-Zeeman reservoir by the rate constants k_C and k_H, respectively and all three are also coupled to the lattice by the spin-lattice relaxation-rate constants R_H, R_C, and R_e. If microwave irradiation is turned on, the electron non-Zeeman reservoir is coupled to the cooling bath by the rate constant R_{CL}. The cooling bath *CL* is assumed to have always a lower temperature than the lattice *L* ($T_{CL} < T_L$) and it is assumed that the lattice has an infinite heat capacity and, therefore, a constant inverse spin temperature β_L. Finally, the ability to turn on and off the microwave irradiation is included by the possibility to decouple *NZ* from *CL*.

The energy-conserving rate equations of heat exchange between the reservoirs can be formulated in analogy to classical thermodynamics. Such an approach leads to a set of three coupled differential equations that describe the time dependence of the inverse spin temperatures of *CZ*, *HZ*, and *NZ*:

$$\begin{aligned}
\dot{\beta}_C(t) &= -k_C\beta_C(t) + k_C\beta_e(t) - R_C[\beta_C(t) - \beta_L] \\
\dot{\beta}_H(t) &= -\frac{c_C}{c_H}k_H\beta_H(t) + \frac{c_C}{c_H}k_H\beta_e(t) - R_H[\beta_H(t) - \beta_L] \\
\dot{\beta}_e(t) &= \frac{c_C}{c_e}k_C\beta_C(t) + \frac{c_C}{c_e}k_H\beta_H(t) - \frac{c_C}{c_e}(k_C + k_H)\beta_e(t) - R_e[\beta_e(t) - \beta_L] + R_{CL}[\beta_{CL}(t) - \beta_e(t)]
\end{aligned} \tag{1}$$

with the heat capacities given by the Curie constants $C_i = \frac{N_i}{4}\gamma_i^2\hbar$, where N_i is the number of spins of nucleus i, the rate constants k_C and k_H describing the heat transfer between the electron non-Zeeman and the two nuclear Zeeman reservoirs. In matrix form the equations can be rewritten in terms of the enhancement factors $\epsilon_i = \frac{\beta_i}{\beta_L}$

$$\dot{\epsilon}(t) = \begin{pmatrix} \frac{\dot{\beta}_C(t)}{\beta_L} \\ \frac{\dot{\beta}_H(t)}{\beta_L} \\ \frac{\dot{\beta}_e(t)}{\beta_L} \end{pmatrix} = \begin{pmatrix} -k_C - R_C & 0 & +k_C \\ 0 & -\frac{c_C}{c_H}k_H - R_H & +\frac{c_C}{c_H}k_H \\ +\frac{c_C}{c_e}k_C & +\frac{c_C}{c_e}k_H & -R_{CL} - R_e - \frac{c_C}{c_e}(k_C + k_H) \end{pmatrix} \cdot \epsilon(t) + \begin{pmatrix} R_C \\ R_H \\ R_e + R_{CL}\epsilon_{CL} \end{pmatrix}. \tag{2}$$

An additional assumption has to be made for the heat capacity C_e of the *NZ* system. Since *NZ* represents the broadened ESR line and to simplify the expression $\frac{c_C}{c_e}$, the heat capacity was assumed to be equal to the Curie constant of a spin - $\frac{1}{2}$ system with a Zeeman splitting according to the electron ESR line width of ≈ 300 MHz. Therefore:

$$C_e = \frac{N_e}{4}\gamma_{NZ}^2\hbar \qquad \text{with} \qquad \gamma_{NZ} = \frac{300}{35}\gamma_C \tag{3}$$

with the ^{13}C Larmor frequency being 35 MHz at 3.4 T and the number of radicals N_e. The cross-polarization process is not described by these equations but will just lead to a change in the initial conditions of the nuclear polarizations or nuclear spin temperatures.

3. Experimental

All experiments were performed with the sample covered by liquid helium, at 4.2 K and ambient pressure. The choice of 4.2 K for the experiments instead of the more typical 1.3 K for dissolution experiments was motivated by the higher temperature stability under these conditions and by the lower helium consumption during the large number of experiments needed to optimize and characterize the CP conditions. All experimental DNP enhancement factors ϵ where calculated as the ratio of the NMR signal (integral under the peak) during the polarization process compared to the NMR signal at thermal equilibrium.

3.1 Sample preparation

For all experiments, samples were used containing 4.5 M [^{13}C]urea (uniformly protonated, Sigma Aldrich) in solvent mixtures of $(1/1)_{vol}$ glycerol/water doped with 20 or 50 mM TEMPO (2,2,6,6-tetramethyl-1-piperidinyloxy, Sigma Aldrich). 100 µl of each solution were sonicated and vortexed prior to loading into the sample container. The filled sample containers were then pre-frozen in liquid nitrogen to ensure glass forming. The sample container consists of a closed PTFA cylinder of 100 µm wall thickness permitting efficient cooling of the sample during the DNP process. Samples have been prepared with different deuteration degrees of the solvent as shown in Table 1.

Table 1: Sample compositions. All samples contain 4.5 M [^{13}C]urea and 20 or 50 mM TEMPO. The difference between solvent and sample deuteration arises from the fully protonated urea.

Sample	Solvent deuteration	Sample deuteration	Solvent $(1/1)_{vol}$	Radical Concentration [mM]
A	0 %	0 %	glycerol/H_2O	50
B	20 %	42 %	glycerol/D_2O	50
B1	20 %	42 %	glycerol/D_2O	20
C	50 %	58 %	glycerol-d3/D_2O	50
D	100 %	85 %	glycerol-d8/D_2O	50

3.2 DNP polarizer

The cryogenic setup of the DNP polarizer is based on a flow-type variable-temperature-insert (VTI) cryostat and is described in detail elsewhere.[10] The DNP probe is home built for static solid-state DNP experiments at 94 GHz ESR frequency (corresponding to a magnetic field of 3.35 T) and temperatures down to 1.3 K. Its skeleton is a single glass-fiber tube (18 mm inner diameter, 1 mm wall thickness) to reduce thermal conductivity to the helium-temperature space. An overview of the sample-space area of the probe is shown in Fig. 2.

A microwave source (Model VCOM-10/94/200-DP, ELVA-1) is located next to the polarizer. It can provide up to 170 mW of continuous-wave power at frequencies between 93.500 and 94.500 GHz.

The microwaves are guided into the cryostat through a WR28 copper waveguide. The last 60 cm of the waveguide to the sample space are made from stainless steel to reduce thermal heating. Immediately above the sample, the WR28-waveguide is converted to a circular 4 mm waveguide. At the magnetic field of 3.35 T, the ESR wavelength is 3.2 mm and the dominant mode in the circular waveguide is $TE_{1,1}$ with its electric field oriented radially with the magnet symmetry. In this mode the 90° elbow guides the microwaves to the sample with less than 1 dB losses. The axis of the waveguide-elbow ending and the direction of microwave propagation is along the axis of the NMR solenoid.

The NMR coil consists of a solenoid with 4 mm inner diameter, ten windings, and is made of 0.6 mm Cu-wire. The sample container has 4 mm outer diameter and is inserted directly into the coil. The NMR circuit is based on the McKay design.[37] The NMR transmission line (inner and outer conductor: Cu), with the NMR coil and sample container attached to it, is inserted into the system through the central glass-fiber tube. This allows changing of samples without warming of the entire probe and can be done at any temperature above 4.2 K and ambient pressure.

The circuit is double-tuned to 142 MHz (^{1}H) and 35 MHz (^{13}C) by tuning and matching components located outside the probe at ambient temperature (Q(^{1}H) = 84, Q(^{13}C) = 36). Due to the simple probe design without dissolution capabilities, the probe allows rf-field amplitudes corresponding to a nutation frequency of 100 kHz using 280 W on the proton and 270 W on the carbon channel. The NMR experiments are controlled by an OPENCORE NMR spectrometer.[38]

3.3 Hartmann-Hahn pulse sequences

For adiabatic conversion of longitudinal to transverse magnetization (sweep-in), hyperbolic-secant pulses[19, 20] were chosen with an amplitude shape of $|\omega_1(t)| = \omega_1^0 \operatorname{sech}(\alpha t)$ and a modulation of the rf frequency of $\Delta\omega(t) = A\tanh(\alpha t)/\tanh(\alpha)$ where *A* describes the amplitude of the frequency sweep and α the truncation level. The effective 90° rotation of the magnetization is achieved by limiting the hyperbolic-secant function to the first half of the pulse. For regenerating Zeeman polarization (sweep-out) after the CP mixing period in order to store the gained polarization along the z-axis, the same hyperbolic-secant pulse was used, however, reversed in time. Both pulses will be referred to as *adiabatic half-passage pulses* (AHP). The frequency sweep range, truncation, and duration of the pulses were optimized using a sequence of sweep-in pulse, 500 µs spin lock (SL), and sweep-out pulse.

The CP sequences using hard 90° pulses and AHP are shown in Fig. 3 and will be referred to as DNP–CP sequences. Both start with a saturation period on both nuclei preceding a variable DNP build-up period, t_{DNP}, followed by the CP sequence block and the readout (Fig. 3a). The CP sequence blocks are [90° – SL – -90°] and [sweep-in – SL – sweep-out] for hard 90° and AHP, respectively (Fig. 3b). For $T_{1\rho}$ measurements, the DNP–CP sequences are modified by omitting the CP block from the channel not used.

The Hartmann-Hahn match was optimized for each of the two DNP–CP implementations (Fig. 3b) separately using a mixing time of τ_{mix} = 1 ms and t_{DNP} = 10 s. The comparison of the AHP with the hard 90° pulses was done using the pulse sequence employed for $T_{1\rho}$ measurements with t_{DNP} = 30 s.

Microwaves were irradiated on the optimum DNP condition throughout the entire experiment. Based on the experimentally determined Hartmann-Hahn conditions, the CP mixing time τ_{mix} was optimized independently for both implementations of the DNP–CP sequence using t_{DNP} = 30 s.

The dependence of the CP efficiency of both sequences on the rf-field strength was analyzed by measuring the CP mixing time curves on sample B after 30 s DNP build up for 20, 50, and 100 kHz rf-field amplitudes during CP. Such high amplitudes can usually not be realized in dissolution DNP probes. They are only reached in the current probe because of the dedicated probe design without dissolution capabilities. The same rf-field amplitude was used as the peak field strength during the AHP pulses. Both sequences were optimized separately at each field strength. In all optimization and characterization measurements the NMR spectra were acquired with four phase-cycled averaged FIDs, each with a 45° excitation pulse.

3.4 Polarization-transfer sequence via dipolar order

The polarization transfer via dipolar order is realized with linear frequency-swept low-power rf pulses with constant amplitude and is demonstrated in this work on sample B1 (Table 1). Figure 4 illustrates the utilized pulse sequence as suggested by Lee et al.,[22] which will be referred to as *laboratory frame de- and remagnetization enabled CP* (LAFDR-CP). The polarization transfer relies on a demagnetization of the proton spin system by a first pulse sweeping from off- to on-resonance on the ^{1}H channel generating dipolar order. A second remagnetization pulse on the ^{13}C channel sweeping from on- to off resonance converts the dipolar order to carbon Zeeman magnetization. Due to the latter step no additional 90° pulse is necessary on carbons at the end of the sequence, as used in the Hartmann-Hahn CP sequences (Fig. 3).

The pulse sequence was roughly optimized by varying the pulse lengths and frequency sweeping ranges (data not shown, ^{1}H: 5 ms pulse length, 100 kHz sweep range and ^{13}C: 20 ms, 80 kHz sweep range). The pulses were realized using the frequency-sweeping mode of the DDS in the OPENCORE spectrometer with a resolution of 1 µs.

3.5 Solution of DGL

The kinetics assumed in the model leads to a set of three coupled differential equations with seven parameters shown in Eq. 2: $R_C, R_H, R_e, k_C, k_H, R_{CL}$, and ϵ_{CL}. The differential equations are numerically solved for an arbitrarily chosen set of seven parameters with the boundary conditions being the starting conditions of the kinetics of the model. All equation-solving and optimization steps were realized with MATLAB, MathWorks™.

For each given sample, the numerical solution routine (function *ode15s*) utilizes an additional unique set of three fixed parameters defining the relative heat capacities of the three spin systems as defined in Eq. 2. The relative heat capacities are calculated with the corresponding Curie constants $\frac{c_i}{c_C} = \frac{N_i}{N_C}\frac{\gamma_i^2}{\gamma_C^2}$, where the ratio of molarity of the nuclei in each sample was used instead of the total number N_i of spins. For situations in which the microwave irradiation is turned off, the cooling rate R_{CL} is set to zero.

To fit the model to the experimental data, by varying the set of parameters, the numerical solutions were fit simultaneously to 12 data sets: the polarization enhancement build-up and decay curves of protons and carbons of samples A, C, and D (see Table 1) each with the appropriate starting conditions ($2 \cdot 2 \cdot 3 = 12$ curves). All data were acquired with four phase-cycled averaged FIDs, each with a 1° or 3.6° excitation pulse for ^{1}H and ^{13}C, respectively. The fitting was realized by minimizing the sum of the 12 norms of the differences between data points and model predictions, henceforth referred to as the goodness of the fit. Finally, the minimization routine was run 150 times with varying randomly chosen starting sets of the seven parameters to minimize the risk of finding local minima.

4. Results and Discussion

4.1 Comparison of AHP and hard-90° Hartmann-Hahn CP

All experiments for characterization and comparison of the Hartmann-Hahn CP sequences were conducted on sample B (see Table 1). To characterize the rotating-frame relaxation times and the magnetization losses due to the projection of the magnetization onto the spin-lock field given by imperfect 90° rotations, time-dependent spin-lock measurements for the sequence with hard 90° pulses and for the sequence with AHP were carried out at the maximum rf-field strength of 100 kHz. The measured $T_{1\rho}$ values under both excitation schemes are comparable for the two nuclei and plotted as the fraction of a reference signal without the CP block in Fig. 5a.

For both nuclei the $T_{1\rho}$ measurement using 90° pulses shows losses of about 10% compared to the reference signal (Fig. 5a). Using the adiabatic-pulse scheme the losses are reduced to 5% and 0% for ^{1}H and ^{13}C, respectively. The losses on ^{1}H could not be eliminated entirely under the condition of the peak rf-field amplitude of the hyperbolic-secant pulse being limited to 100 kHz. The reasons for this loss are the strong homonuclear dipolar couplings of the ^{1}H spin system (FWHM ~70 kHz), which reduces the adiabaticity during the hyperbolic-secant pulse. The higher losses in the sequence using hard pulses are attributed to imperfect 90° rotations due to rf-field inhomogeneity over the sample, to significant resonance-offset effects, and subsequent losses due to a projection of the magnetization onto the spin-lock field.

Having characterized the behavior under spin lock we now turn to the CP experiment. The build up of the polarization as a function of the CP mixing time at 100 kHz field strength is shown in Fig. 5b. At the optimum mixing time of τ_{mix} = 1 ms, the CP sequence with AHP gives a signal which is about 15% higher than the signal of the sequence using hard 90° pulses. The larger increase in CP efficiency of 15% compared to the increase in plain excitation efficiency of 10% presented in the $T_{1\rho}$ measurements is assumed to arise from cross polarization during the amplitude and frequency sweeping of the AHP.

Figure 6 shows the characteristic CP enhancement factors of both CP sequences as function of the spin-lock and peak AHP rf-field strength which is an important indicator of the viability in rf-restricted dissolution DNP–CP probes. The data shows a decrease in the CP factor for both sequences. However, the relative difference between the CP factors increases up to 40% at 20 kHz. These results

demonstrate the advantage of using AHP compared to hard pulses in Hartmann-Hahn CP especially at low rf-field amplitudes.

4.2 LAFDR–CP

The polarization transfer efficiency of the LAFDR–CP can be enhanced by an overlap of the two frequency-swept pulses. The increase reaches up to 23% in the given sample (Fig. 7a). The reason is assumed to be the short relaxation time of the homonuclear dipolar order generated by the proton frequency-swept pulse. By varying t_D in the LAFDR-CP pulse sequence (Fig. 4) this dipolar relaxation time was measured to be 13.7 ± 0.7 ms in the given sample (B1). It was found to decrease with higher radical concentrations. The short relaxation times was the reason for the choice of sample B1 to demonstrate the LAFDR–CP in combination with DNP, however, a stringent investigation of the dependencies on all sample parameters has not yet been undertaken.

The transfer efficiency was optimized with respect to the rf amplitude on both channels independently (Fig. 7b) with an optimum at 3 kHz for protons and 10 kHz for carbons. Relative to the optimum rf amplitudes, the regions in which the transfer efficiency decreases by less than 10% are roughly ±60% for protons and ±30% for carbons. The LAFDR-CP sequence is, therefore, significantly less sensitive to B_1 inhomogeneities compared to the Hartmann-Hahn CP methods (±4%, compare Fig. 7c).

With the optimized LAFDR-CP sequence a DNP–CP build up was acquired on sample B1 as shown in Fig. 8. A final CP enhancement of $\epsilon_{CP} = 1.5$ at the DNP steady state was obtained (see Fig. 8). If the rf-field strengths in DNP probes are limited to below 10 kHz the LAFDR-CP sequence is, therefore, superior compared to the Hartmann-Hahn CP method.

4.3 Thermal-mixing model predictions and solvent deuteration

To obtain the parameters for the thermodynamic model, the ^{1}H and ^{13}C DNP build-up curves and the relaxation to thermal equilibrium for three different deuteration degrees (for details see also Section 3.5 and Fig. 9) were used. With 150 randomly chosen starting values of the free parameters, the fitting process leads to a set of 150 solutions. The set of parameters for the best fit is given in Table 1 and the experimental data sets together with the best fit are shown in Fig. 9.

Table 2: Parameters of the best fit. The error given for each parameter is the standard deviation of the 108 solutions within a range of 4% compared to the best fit.

R_C	R_H	R_e	k_C	k_H	R_{CL}	ε_{CL}
$0.0012\ s^{-1}$	$0.014\ s^{-1}$	$0.0013\ s^{-1}$	$0.007\ s^{-1}$	$26.11\ s^{-1}$	$5.1\ s^{-1}$	198.49
$\pm\ 0.0001\ s^{-1}$	$\pm\ 0.0002\ s^{-1}$	$\pm\ 0.03\ s^{-1}$	$\pm\ 0.0002\ s^{-}$	$\pm\ 9.75\ s^{-1}$	$\pm\ 0.14\ s^{-1}$	$\pm$ 4.16
($T_{1C} =$ 864.7 s)	($T_{1H} =$ 71.3 s)	($T_{1NZ} =$ 749.9 s)				

The fitted common set of parameters solves the model simultaneously for the 3 samples A, C, and D (see Table 1) with different deuteration degree (Fig. 9) by modification of the heat capacity of the

proton bath solely. With the fitted set of parameters, the behavior of the fourth sample (B) with a different deuteration degree could be predicted both in build-up and relaxation speed as well as in steady-state DNP enhancement on both nuclei (Fig. 10). Only the heat capacity of the proton bath has to be modified corresponding to the actual molarity of proton nuclei in the sample. Note that the relaxation rate of the NZ bath, $R_e = T_{1\mathrm{NZ}}^{-1}$, is not to be misunderstood as the electron spin-lattice relaxation rate. The variance on this parameter is large and almost equal results are obtained for values down to $T_{1\mathrm{NZ}} = 10\ s$ such that the obtained value for R_e is not assumed to be unrealistic but rather unsubstantial. The exact values of the parameters found in the best fit are not the focus of this work and shall therefor not be further discussed quantitatively at this point.

The model correctly predicts the behavior of both ^{1}H and ^{13}C polarization after arbitrary experimental preparation of both nuclear spin temperatures, with and without microwave irradiation (Fig. 11a – d). Specifically, it anticipates that after a CP pulse the ^{13}C enhancement tends to re-equalize with the ^{1}H enhancement within the thermal mixing time T_{TM} (Fig. 11a). This time constant depends on the coupling strength of *NZ* to both nuclear Zeeman baths and is in general faster than the nuclear T_1 (also clearly apparent in Fig. 11b and d). Figure 11b shows that at 4.2 K the thermal mixing process is active even without ongoing microwave irradiation. In agreement to the findings by Cox et al. in 1973[39] it shows that the ^{13}C polarization rises after a saturation train. This behavior is well predicted by the introduced model and clearly confirms that the thermal-mixing model describes the time-dependence of the polarization well.

The implication of the fast thermal mixing evident from Fig. 11a and 14b to DNP–CP is that the ^{13}C polarization decays fast after the CP pulse even if the microwaves are turned off. This is a property of TM and is a drawback for DNP–CP. For this an ideal system would have minimal coupling between *CZ* and *NZ* and maximum coupling between *HZ* to *NZ*.

In Fig. 11c the CP pulse is applied at a time point, such that the resulting ^{13}C polarization equals the steady-state DNP enhancement. Here, the model correctly anticipates the decrease of polarization to re-equalize both carbon and proton enhancements. This shows that enhancing the carbon polarization to its steady-state DNP value with a single DNP–CP pulse will not lead to a steady state. Finally, Fig. 11d illustrates how the ^{13}C polarization is affected by (partial) saturation of the ^{1}H polarization as will occur during the CP step. The ^{13}C spin temperature clearly depletes until it re-equalizes with the recovering ^{1}H spin temperature.

It is worth to mention that the model also correctly predicts the initial DNP build-up behavior of both spin baths. While the ^{1}H polarization builds up in a mono-exponential manner, the ^{13}C polarization was found to have a reduced initial build up rate (Fig. 9, 10). In the terminology of the spin-thermodynamic model the reason for this is the much weaker coupling between *CZ* and *NZ* compared to the coupling between *HZ* and *NZ*.

5. Conclusion

We have discussed in this contribution the combination of DNP to ^{1}H with subsequent ^{1}H-^{13}C polarization transfer for dissolution DNP. We showed that the thermal-mixing mechanism is suited for DNP–CP since it allows to enhance the polarization of high-γ nuclei to the same extend as the low-γ

nuclei. At the same time, the presented thermal mixing model illustrates the intrinsic drawback of thermal mixing for DNP–CP, i.e., the indirect coupling of the nuclear spin temperatures. A consequence of this coupling is that the possibly deflated high-γ nuclei after CP quickly heat the CP-enhanced low-γ nuclei. Thus, for dissolution DNP–CP experiments sample compositions are desired that feature a weak coupling of the electron non-Zeeman bath to the low-γ nuclei while having strong coupling to the high-γ nuclei allowing for fast initial DNP build up but slow thermal mixing after the CP pulse.

We have shown that utilizing adiabatic-half passage pulses can be beneficial for the application in DNP–CP using Hartmann-Hahn cross-polarization sequences. Specifically, they outperform conventional hard pulses if the available rf-field strength is limited. Up to 40% enhancement was found at an rf-field strength of 20 kHz. Such low rf-field amplitudes are often found in dissolution DNP–CP probes.

If the rf performance is further limited to bellow 10 kHz and the geometry of the DNP probe does not allow homogeneous B_1 excitation profiles, it was shown that frequency-swept de- and remagnetization pulses allow polarization transfer with an enhancement factor of 1.5 and, thus, are superior to the investigated Hartmann-Hahn CP methods under such conditions.

A spin-thermodynamic model based on the thermal-mixing DNP mechanism was applied to the spin system. By varying the thermal capacity of the proton Zeeman bath the model is capable of fitting the DNP build up as well as the T_1 decay simultaneously for a series of samples with varying protonation degree and, thus, correctly predicts the effect of solvent deuteration. It provides an intuitive understanding of the reason for the enhanced DNP efficiency upon sample deuteration demonstrated here.

The presented model, furthermore, correctly predicts the course of the spin temperatures after preparation of an arbitrary initial state. Particularly, the course of the low-γ polarization after a CP pulse is of interest for the combination of DNP–CP with subsequent dissolution. It was demonstrated that the equilibration of both low and high-γ polarization after the CP pulse is faster than the low-γ spin-lattice relaxation rate.

Acknowledgement

We would like to thank Rene Tschaggelar for the support in building the microwave circuit and design of the waveguide components. The work has been supported by following grants: ETH TH-19 07-3, SNF CR23I3_132671, and COST TD1103.

References

1. A. Abragam and M. Goldman, *Rep. Prog. Phys.*, 1978, **41**, 395-467.
2. J. H. Ardenkjaer-Larsen, B. Fridlund, A. Gram, G. Hansson, L. Hansson, M. H. Lerche, R. Servin, M. Thaning and K. Golman, *Proc. Natl. Acad. Sci. USA*, 2003, **100**, 10158-10163.
3. F. A. Gallagher, M. I. Kettunen and K. M. Brindle, *Prog. Nucl. Magn. Reson. Spectrosc.*, 2009, **55**, 285-295.
4. A. L. Davis and I. J. Day, in *eMagRes*, John Wiley and Sons, Ltd, 2007.
5. K. M. Brindle, S. E. Bohndiek, F. A. Gallagher and M. I. Kettunen, *Magnetic Resonance in Medicine*, 2011, **66**, 505-519.
6. K. Golman, J. H. Ardenaer-Larsen, J. S. Petersson, S. Mansson and I. Leunbach, *Proc. Natl. Acad. Sci.*, 2003, **100**, 10435-10439.
7. J. H. Ardenkjaer-Larsen, K. Golman, R. in't Zandt, M. Lerche and R. Pehrson, *Cancer Research*, 2006, **66**, 10855-10860.
8. K. Weiss, E. Mariotti, D. Hill, M. Orton, J. Dunn, R. Medina, R. Southworth, S. Kozerke and T. Eykyn, *Appl. Magn. Reson.*, 2012, **43**, 275-288.
9. A. Comment, B. van den Brandt, K. Uffmann, F. Kurdzesau, S. Jannin, J. A. Konter, P. Hautle, W. T. H. Wenckebach, R. Gruetter and J. J. van der Klink, *Concepts in Magnetic Resonance Part B-Magnetic Resonance Engineering*, 2007, **31B**, 255-269.
10. M. Batel, M. Krajewski, K. Weiss, O. With, A. Daepp, A. Hunkeler, M. Gimersky, K. P. Pruessmann, P. Boesiger, B. H. Meier, S. Kozerke and M. Ernst, *J. Magn. Reson.*, 2012, **214**, 166-174.
11. F. Kurdzesau, B. van den Brandt, A. Comment, P. Hautle, S. Jannin, J. J. van der Klink and J. A. Konter, *J. Phys. D Appl. Phys.*, 2008, **41**, 155506.
12. L. Lumata, M. E. Merritt, C. R. Malloy, A. D. Sherry and Z. Kovacs, *J Phys Chem A*, 2012, **116**, 5129-5138.
13. S. R. Hartmann and E. L. Hahn, *Phys. Rev.*, 1962, **128**, 2042-2053.
14. A. Linde, University of Nottingham, 2009.
15. S. Jannin, A. Bornet, S. Colombo and G. Bodenhausen, *Chem. Phys. Lett.*, 2011, **517**, 234-236.
16. M. Batel, M. Krajewski, A. Daepp, A. Hunkeler, B. H. Meier, S. Kozerke and M. Ernst, *Chem. Phys. Lett.*, 2012, **554**, 72-76.
17. S. Jannin, A. I. Bornet, R. Melzi and G. Bodenhausen, *Chem. Phys. Lett.*, 2012, **549**, 99-102.
18. A. Bornet, R. Melzi, A. J. P. Linde, P. Hautle, B. van den Brandt, S. Jannin and G. Bodenhausen, *J Phys Chem Lett*, 2013, **4**, 111-114.
19. M. S. Silver, R. I. Joseph, C. N. Chen, V. J. Sank and D. I. Hoult, *Nature*, 1984, **310**, 681-683.
20. A. Tannus and M. Garwood, *J. Magn. Reson., Ser. A*, 1996, **120**, 133-137.
21. A. Pines and T. W. Shattuck, *J. Chem. Phys.*, 1974, **61**, 1255-1256.
22. J. S. Lee and A. K. Khitrin, *J. Magn. Reson.*, 2005, **177**, 152-154.
23. J. S. Lee and A. K. Khitrin, *J. Chem. Phys.*, 2008, **128**, 114504.

24. A. W. Overhauser, *Phys. Rev.*, 1953, **92**, 411-415.
25. R. A. Wind, M. J. Duijvestijn, C. van der Lugt, A. Manenschijn and J. Vriend, *Prog. Nucl. Magn. Reson. Spectrosc.*, 1985, **17**, 33-67.
26. C. D. Jeffries, *Phys. Rev.*, 1957, **106**, 164-165.
27. A. Abragam and W. G. Proctor, *Cr Hebd Acad Sci*, 1958, **246**, 2253-2256.
28. Y. Hovav, A. Feintuch and S. Vega, *J. Magn. Reson.*, 2010, **207**, 176-189.
29. Y. Hovav, A. Feintuch and S. Vega, *J. Magn. Reson.*, 2012, **214**, 29-41.
30. A. B. Barnes, G. De Paepe, P. C. A. van der Wel, K. N. Hu, C. G. Joo, V. S. Bajaj, M. L. Mak-Jurkauskas, J. R. Sirigiri, J. Herzfeld, R. J. Temkin and R. G. Griffin, *Appl. Magn. Reson.*, 2008, **34**, 237-263.
31. V. Vitzthum, M. A. Caporini and G. Bodenhausen, *J. Magn. Reson.*, 2010, **205**, 177-179.
32. A. G. Redfield, *Phys. Rev.*, 1955, **98**, 1787-1809.
33. S. T. Goertz, *Nuclear Instruments and Methods in Physics Research Section a-Accelerators Spectrometers Detectors and Associated Equipment*, 2004, **526**, 28-42.
34. J. Heckmann, W. Meyer, E. Radtke, G. Reicherz and S. Goertz, *Phys. Rev. B*, 2006, **74**, 134418.
35. D. Shimon, Y. Hovav, A. Feintuch, D. Goldfarb and S. Vega, *Phys. Chem. Chem. Phys.*, 2012, **14**, 5729-5743.
36. M. Goldman, S. F. J. Cox and V. Bouffard, *Journal of Physics C-Solid State Physics*, 1974, **7**, 2940-2952.
37. M. S. Conradi, *Concepts Magn. Reson.*, 1993, **5**, 243-262.
38. K. Takeda, *Rev. Sci. Instrum.*, 2007, **78**, 033103.
39. S. F. J. Cox, V. Bouffard and M. Goldman, *Journal of Physics C-Solid State Physics*, 1973, **6**, L100-L103.

Figure Captions:

Figure 1 Spin-thermodynamic model with the heat flow and the inverse spin temperatures β. The ^{13}C Zeeman reservoir (*CZ*), ^{1}H Zeeman reservoir (*HZ*), and the electron non-Zeeman reservoir (*NZ*) relax to the lattice (*L*) with relaxation rate constants R_C, R_H, and R_e, respectively. *NZ* is coupled to both *CZ* and *HZ* with the thermal rate constants k_C and k_H and gets cooled via the microwave-induced cooling rate R_{CL} from the cooling reservoir (*CL*).

Figure 2 Lower end of the DNP probe. The stainless-steel WR28 waveguide (1) connects to the rectangular-to-circular waveguide converter (2). A circular 90° waveguide elbow (3) guides the microwaves to the sample container loaded directly to the NMR coil (4). A capacitive cylindrical helium-level sensor (5) is used to monitor the liquid-helium level in the cryostat. The entire probe construction is based on a central glass-fiber tube (6), additionally acting as guiding port for the NMR stick (transmission line with NMR coil attached).

Figure 3 DNP–CP sequence. a) The DNP–CP sequence starts with a saturation pulse train on both nuclei, followed by the DNP build-up period with variable duration t_{DNP}. The CP block is followed by the read out, consisting in this work of four phase-cycled acquisitions. The microwaves are tuned to the optimum positive DNP condition and kept on during the entire experiment. b) The CP blocks use hard 90° pulses and adiabatic half-passage pulses for rotation of the magnetization.

Figure 4 LAFDR-CP pulse sequence. A linear frequency-swept pulse with constant amplitude on the proton channel (optimized sweep: -100 kHz off-resonant to on-resonance) is followed by a variable delay time t_D and a linear frequency-swept pulse with constant amplitude on the carbon channel (sweeping from on-resonance to -80 kHz off-resonance). The delay t_D is used to measure the dipolar relaxation time and allows to optimize the pulse sequence by accepting negative values for an overlap of the frequency-swept pulses.

Figure 5 $T_{1\rho}$ measurements and polarization transfer dependence on the mixing time on sample B for both nuclei and both Hartmann-Hahn CP implementations (Fig. 3b) with t_{DNP} = 30 s. The DNP–CP sequences (Fig. 3) were used omitting the CP block on the channel not used. (a) The $T_{1\rho}$ data is given as ratio to a reference spectrum after 30 s DNP build up without CP block. All decays were approximated with a bi-exponential function with the parameters for ^{1}H: $T_{1\rho,a}$ = 9.9±0.7 ms, $T_{1\rho,b}$ = 0.7±1.4 ms (hard 90° pulses), and $T_{1\rho,a}$ = 10.0±0.8 ms, $T_{1\rho,b}$ = 0.7±1.4 ms (AHP); for ^{13}C: $T_{1\rho,a}$ = 156.9±20.8 ms, $T_{1\rho,b}$ = 11.9±2.4 ms (hard 90° pulses), and $T_{1\rho,a}$ = 141.1±13.2 ms, $T_{1\rho,b}$ = 9.2±1.4 ms (AHP). (b) The mixing-time curves at a field strength of 100 kHz are presented as the CP factor reached in the case of equal spin temperature and were therefore corrected for the ratio of ^{1}H to ^{13}C polarization after 30 s DNP build up (~ 4.5). The experiment is used to quantify the polarization transfer efficiency of the two Hartmann-Hahn CP implementations.

Figure 6 The CP factor as a function of rf-field strength for both Hartmann-Hahn CP sequences on sample B. In each experiment the CP condition was optimized separately. The inset shows the relative increase of the CP factor of the AHP sequence compared to the hard 90° sequence at each field strength.

Figure 7 (a) Transfer efficiency of the LAFDR-CP sequence as a function of the overlap of the sweep pulses. The resulting ^{13}C signal is shown normalized to the achieved signal with t_D = 0 ms delay between both sweep pulses.(b) B_1-dependence of the LAFDR-CP. The transfer efficiency was measured independently for both ^{1}H and ^{13}C rf amplitudes at t_D = 0 ms overlap of the sweeps. (c) Hartmann-Hahn matching profile for the hard 90° pulse DNP–CP sequence on sample B. With the rf-field amplitude of the ^{1}H channel set to ~ 100 kHz, the CP transfer efficiency was measured with τ_{mix}= 1 ms and t_{DNP} =10 s for different rf-field amplitudes on the ^{13}C channel.

Figure 8 DNP–CP ^{13}C polarization build up using LAFDR-CP. The reference DNP build-up data (solid black) was acquired with low-flip angle pulses during a single DNP build up. The DNP-LAFDR-CP data (red circles) was acquired in successive *saturation – polarization – LAFDR-CP* experiments with variable polarization times. The polarization enhancement at the DNP steady state achieved by the LAFDR-CP transfer is 50% in the given sample (B1).

Figure 9 Experimentally obtained ^{1}H and ^{13}C enhancement curves for samples A, C, and D used to fit the model parameters. The simulated enhancement curves using the best-fit parameters (Table 2) are plotted as solid lines.

Figure 10 Thermodynamic model predictions using the best-fit parameters (Table 2) and experimentally obtained values of the DNP enhancement and decay of sample B. The model used a value for the ^{1}H heat capacity that was adjusted corresponding to the actual molarity of ^{1}H nuclei in the sample.

Figure 11 Thermodynamic model predictions using the best-fit parameters and experimental values of the ^{1}H and ^{13}C enhancement curves of sample A after different preparations. For a guide to the eye the DNP build-up data (a,c,d) and decay data (b) are underlayed in light grey. The model predicts well (solid lines) the enhancement curve of ^{13}C after a CP pulse at $t = 90\ s$ (a), the ^{13}C enhancement course after steady-state DNP followed by a single saturation on ^{13}C and microwaves turned off (b), both enhancement curves after a CP pulse at $t = 20\ s$ (c), and both enhancement curves during DNP build up after a single saturation at $t = 120\ s$ on ^{1}H (d).

Figures:

Figure 1:

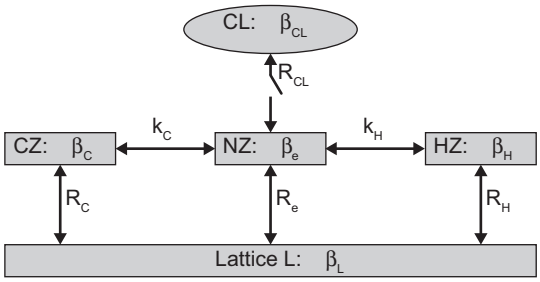

Figure 2:

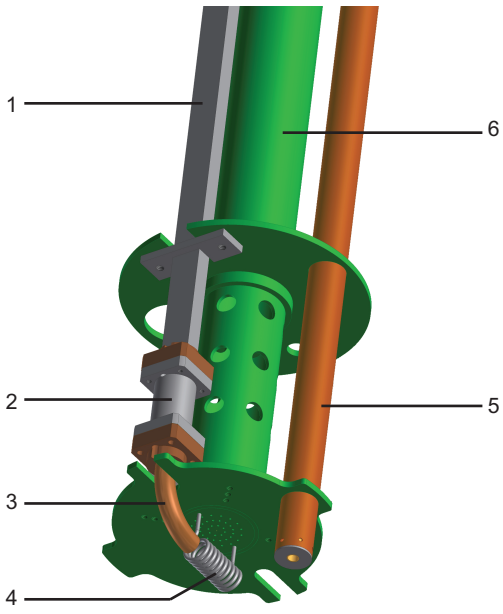

Figure 3:

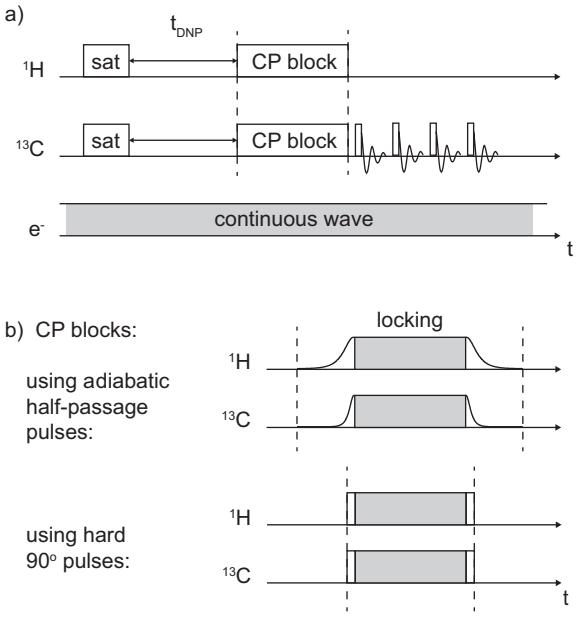

Figure 4:

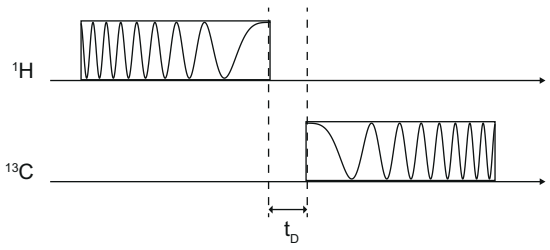

Figure 5:

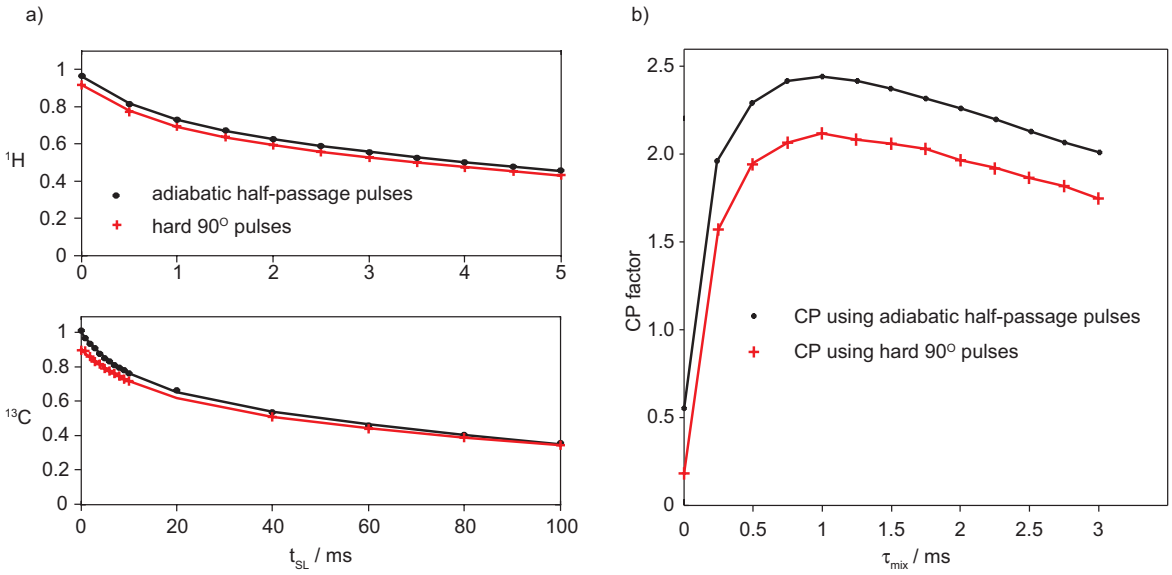

Figure 6:

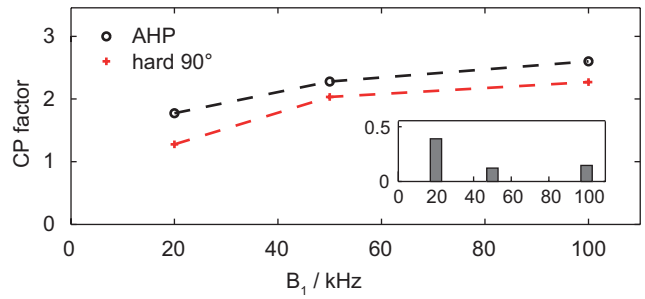

Figure 7:

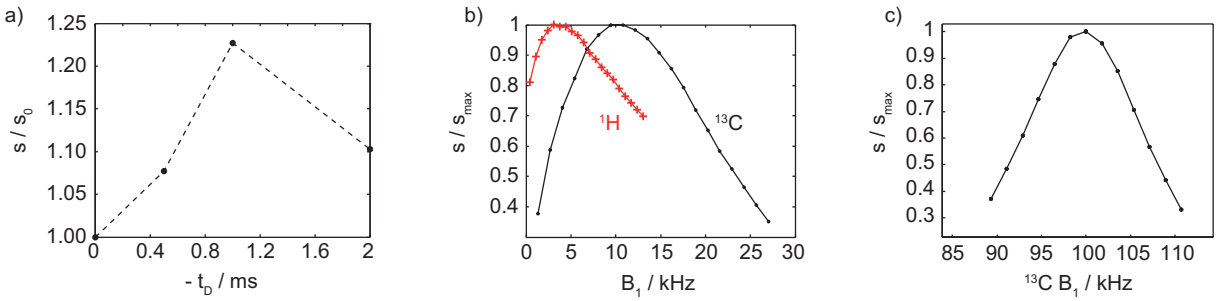

Figure 8:

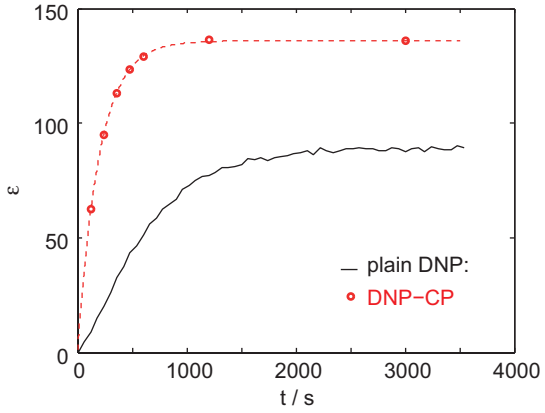

Figure 9:

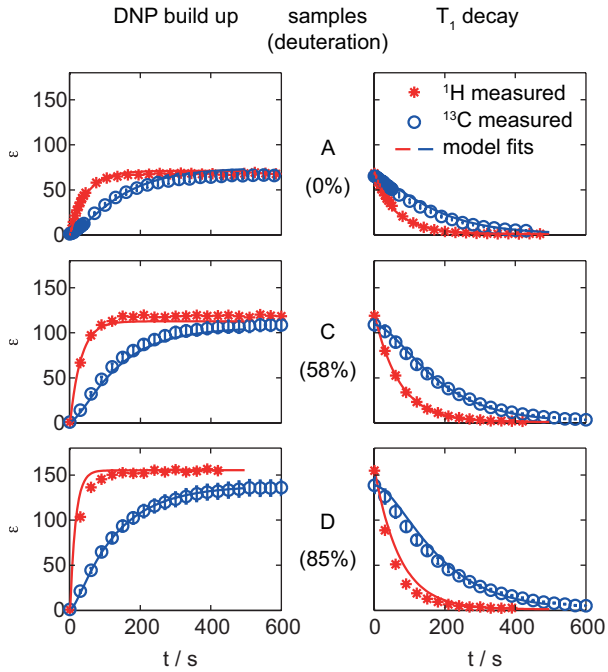

Figure 10:

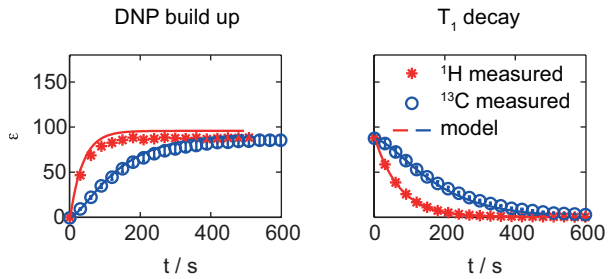

Figure 11: